catalysts

Article

Piezoelectric-Driven Fenton System Based on Bismuth Ferrite Nanosheets for Removal of *N*-acetyl-para-aminophenol in Aqueous Environments

Chi Zhou [1,†], Shenglong Jing [2,†], Teng Miao [1], Nianlai Zhou [1], Hang Zhang [1], Yi Zhang [1], Lin Ge [2], Wencheng Liu [2] and Zixin Yang [2,*]

[1] Hubei Water Resources and Hydropower Science and Technology Promotion Center, Hubei Water Resources Research Institute, Wuhan 430070, China
[2] Department of chemistry, College of Chemistry, Huazhong Agricultural University, Wuhan 430070, China
* Correspondence: zixinyang@mail.hzau.edu.cn
† These authors contributed equally to this work.

Abstract: Emerging pollutants, such as *N*-acetyl-para-aminophenol, pose significant challenges to environmental sustainability, and $Bi_2Fe_2O_2$ (BFO) nanomaterials are an emerging class of piezoelectric materials. This study presents a novel piezoelectric-driven Fenton system based on $Bi_2Fe_4O_9$ nanosheets for the efficient degradation of organic pollutants. BFO nanosheets with varying thicknesses were synthesized, and their piezoelectric properties were confirmed through piezoresponse force microscopy and heavy metal ion reduction experiments. The piezoelectric electrons generated within the BFO nanosheets facilitate the in situ production of hydrogen peroxide, which in turn drives the Fenton-like reaction. Furthermore, the piezoelectric electrons enhance the redox cycling of iron in the Fenton process, boosting the overall catalytic efficiency. The energy band structure of BFO nanosheets is well-suited for this process, enabling efficient hydrogen peroxide generation and promoting Fe^{3+} reduction. The findings demonstrate that thinner BFO nanosheets exhibit superior piezoelectric activity, leading to enhanced catalytic performance. Additionally, the incorporation of gold nanodots onto BFO nanosheets further boosts their piezocatalytic efficiency, particularly in the reduction of Cr (VI). The system exhibited robust oxidative capacity, stability, and recyclability, with reactive oxygen species (ROS) verified via electron paramagnetic resonance spectroscopy. Overall, BFO nanosheets, with their optimal energy band structure, self-supplied hydrogen peroxide, and enhanced Fe^{3+} reduction, represent a promising, sustainable solution for advanced oxidation processes in wastewater treatment and other applications.

Keywords: $Bi_2Fe_4O_9$; piezo-catalysis; fenton reaction; pollutant degradation; *N*-acetyl-para-aminophenol

Academic Editors: Wajid Zaman and Muhammad Saeed Akhtar

Received: 7 December 2024
Revised: 23 January 2025
Accepted: 23 January 2025
Published: 27 January 2025

Citation: Zhou, C.; Jing, S.; Miao, T.; Zhou, N.; Zhang, H.; Zhang, Y.; Ge, L.; Liu, W.; Yang, Z. Piezoelectric-Driven Fenton System Based on Bismuth Ferrite Nanosheets for Removal of *N*-acetyl-para-aminophenol in Aqueous Environments. *Catalysts* **2025**, *15*, 126. https://doi.org/10.3390/catal15020126

1. Introduction

With the development of the pharmaceutical and chemical industries, wastewater containing Personal Care Products (PCCPs), such as *N*-acetyl-para-aminophenol (APAP), presents new challenges for water treatment [1–3]. These emerging pollutants, which possess biological activity, can pose significant risks to human health and ecological systems even at low concentrations [4,5]. Piezo-catalysis is an emerging strategy for generating reactive oxygen species (ROS) by harnessing ambient mechanical energy, without the

need for exogenous oxides [6]. Applied mechanical stress induces a built-in electric field in piezoelectric materials through dipole polarization, which subsequently drives a piezoelectrochemical process at the material-solution interface [7]. In recent years, various piezo-catalytic systems have been developed for selective deposition, hydrogen production [8], hydrogen production [9] and dye degradation [10–12], owing to their high efficiency and cost-effectiveness compared to traditional methods.

Many studies have focused on enhancing piezoelectric properties through material morphological modifications, as materials with the same composition but different structures significantly impact the transfer of electric charges [13]. To ensure efficient charge transfer to the material surface and surrounding molecules involved in electrochemical processes, the chosen material should have limited thickness and a large specific surface area [14]. Thus, nanofabrication of piezoelectric crystals to improve asymmetry has become a growing trend [15]. Wu et al. demonstrated that single-layer and few-layered $MoSe_2$ nanoflowers exhibit significantly higher piezoelectric potential, with a current of up to 250 pA measured using a TUNA probe [16]. They further showed that the piezoelectric potential of nanomaterials is greater than that of bulk particles due to their ease of structural deformation [17]. Building on these ideas, many one-dimensional (1D) and two-dimensional (2D) piezoelectric materials have been developed, such as MoS_2 [18], $BaTiO_3$ nanobelt [19], ZnO nanoparticles [20], and g-C_3N_4 [21].

Current piezoelectric catalysis systems tend to focus on dye degradation, while the removal of emerging pollutants, such as phenolic compounds with more stable chemical structures, requires stronger oxidative stress. To generate hydroxyl radicals with stronger oxidative activity, Lv et al. [22] first proposed a piezo-Fenton system by introducing exogenous ferrous ions into a $BaTiO_3$-based piezoelectric reaction. The piezo-generated hydrogen peroxide was then converted into hydroxyl radicals through the Fenton reaction, demonstrating excellent removal efficiency for aquatic organic acids, including 4-(2-hydroxy-1-naphthylazo)-benzenesulfonic acid sodium, phenol, and 4-chlorophenol. Wei et al. [23] further enhanced the piezo-Fenton process by loading Fe onto the surface of bismuth vanadate (BVO), achieving in situ catalysis for the degradation of p-chlorophenol. These studies confirmed that the piezo-Fenton system is an economical technique for generating large quantities of hydroxyl radicals. However, challenges remain, particularly regarding the degradation of catalytic performance and the secondary pollution caused by the leakage of doped or supported iron species, a common issue in Fenton-Advanced Oxidation Technology [24]. To address this, bismuth ferrite crystals ($Bi_2Fe_4O_9$), which possess inherent Fenton-like catalytic activity under photoexcitation [25], were explored as iron substitutes to achieve more stable and cleaner processes. Whether $Bi_2Fe_4O_9$ can serve as a potential piezoelectric-Fenton catalyst depends on its ability to exhibit piezoelectric activity that aligns with the Fenton process. Interestingly, some studies have found that $Bi_2Fe_4O_9$ nanosheets exhibit piezoelectric activity, despite the fact that the Pbam point group to which $Bi_2Fe_4O_9$ belongs is centrosymmetric and theoretically not associated with piezoelectric effects. For instance, Wang et al. demonstrated the use of the piezoelectric effect of $Bi_2Fe_4O_9$ nanosheets to generate superoxide anions through the reduction of molecular oxygen by piezoelectrons and to activate the decomposition of peroxydisulfate via piezo-promoted regeneration of ferrous ions [26,27]. The study by Cheng et al. suggests that the piezoelectric property of centrosymmetric $Bi_2Fe_4O_9$ nanosheets could stem from the surface polarization due to the exposure of distorted non-centrosymmetric ligands in the unit cell [28].

Herein, we investigated the removal behavior of phenolic compounds by $Bi_2Fe_4O_9$ nanosheets under ultrasonic excitation and elucidated the piezo-Fenton coupling reaction mechanism involved. A series of $Bi_2Fe_4O_9$ nanosheets with varying thicknesses were synthesized via hydrothermal methods. Using piezoresponse force microscopy (PFM) and Cr

(VI) reduction experiments, we observed the piezoelectric effect of $Bi_2Fe_4O_9$ nanosheets and the effect of material thickness on the piezoelectric effect. *N*-acetyl-para-aminophenol (APAP), a phenolic compound, was selected as the model pollutant to evaluate the efficiency of the catalyst in removing pollutants under ultrasonic excitation. Finally, electron paramagnetic resonance (EPR) and free radical scavenger experiments were conducted to identify and validate the role of reactive oxygen species (ROS) during the degradation process, providing a comprehensive understanding of the in situ piezo-Fenton system's mechanism. This study demonstrates the potential of bismuth ferrite nanosheets in constructing a self-sustaining hydrogen peroxide piezo-Fenton system, which can inspire the development of more efficient piezo-Fenton catalysts for applications in environmental and other fields.

2. Results and Discussion

2.1. Synthesis and Characterization of Catalysts

The synthesis steps for a series of $Bi_2Fe_4O_9$ (BFO) materials are shown in Figure 1a. As described in previous reports [29], BFO-1 was synthesized using a simple hydrothermal method with iron nitrate and bismuth nitrate. Based on this approach, we varied the KOH concentration, heating time, and precursor molar ratio during hydrothermal synthesis to prepare three additional BFO materials (BFO-2 to BFO-4) with different thicknesses. In solution, the nanoparticle shape can be controlled by using appropriate capping agents, such as ionic or nonionic organic surfactants, to regulate nanoparticle growth direction [30]. As an alkaline substance and surfactant, KOH can adsorb onto the surface of the BFO crystal (BFO-1, BFO-2, BFO-3), limiting its growth and thus reducing the thickness of the lamellar material. Lower KOH concentrations and longer heating times favor the formation of thicker crystal materials. BFO-1 can reduce $HAuCl_4$ under ultrasonic conditions in the absence of light, leading to the deposition of Au nanoparticles on the material, resulting in BFO@Au, as shown in Figure 1a.

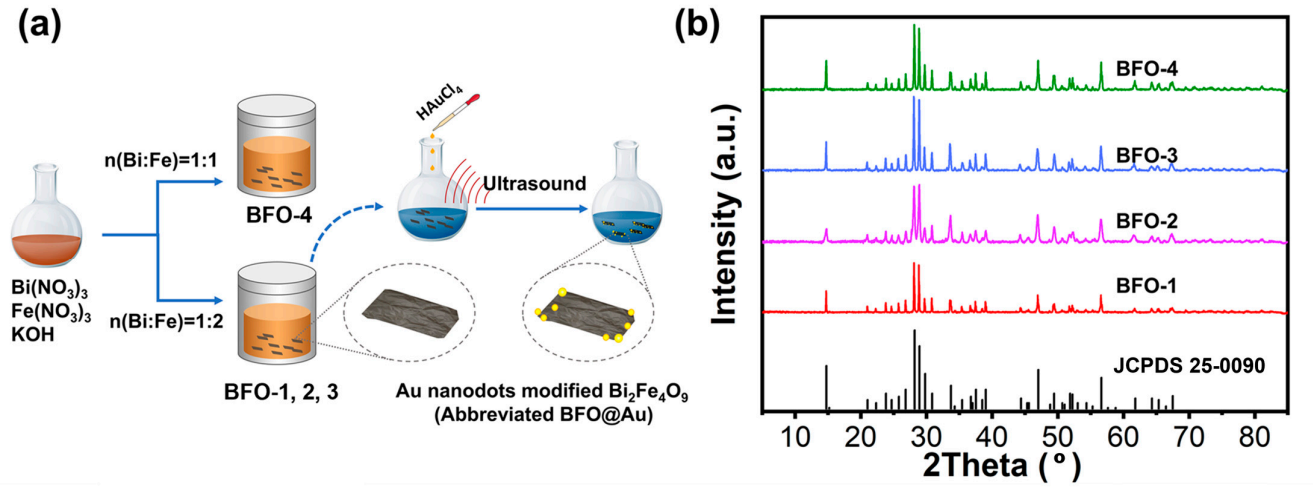

Figure 1. Schematic synthesis (**a**) and corresponding XRD patterns (**b**) of a series of BFO materials.

The XRD pattern of the BFO materials displayed sharp peaks that perfectly matched the standard data for the mullite phase $Bi_2Fe_4O_9$ crystallites (JCPDS: 25-0090) with the Pbam space group (Figure 1b) [26]. The diffraction peaks at 2θ = 14.8°, 28.2°, 28.9°, 47.0°,

and 56.6° correspond to (001), (121), (211), (141), and (332) crystal planes, respectively. Additionally, we tested two reported piezoelectric materials, $BiFeO_3$ and nano-ZnO, for comparison. Nano-ZnO is a commonly used commercial material, while BiFeO3 was synthesized following the procedure described in the literature [31]. Both $BiFeO_3$ (JCPDS: 71-2494) with the R3c space group (Figure S1) and nano-ZnO (JCPDS: 89-0511) with the P63mc space group [32,33] belong to non-centrosymmetric point groups with a piezoelectric effect.

To investigate the thickness of the series of BFO materials, multiple characterization methods were employed, including AFM (Figure S2a and S3) and SEM (Figure 2d,e). The thickness of each material and its estimation method are summarized in the table inserted in Figure 2.

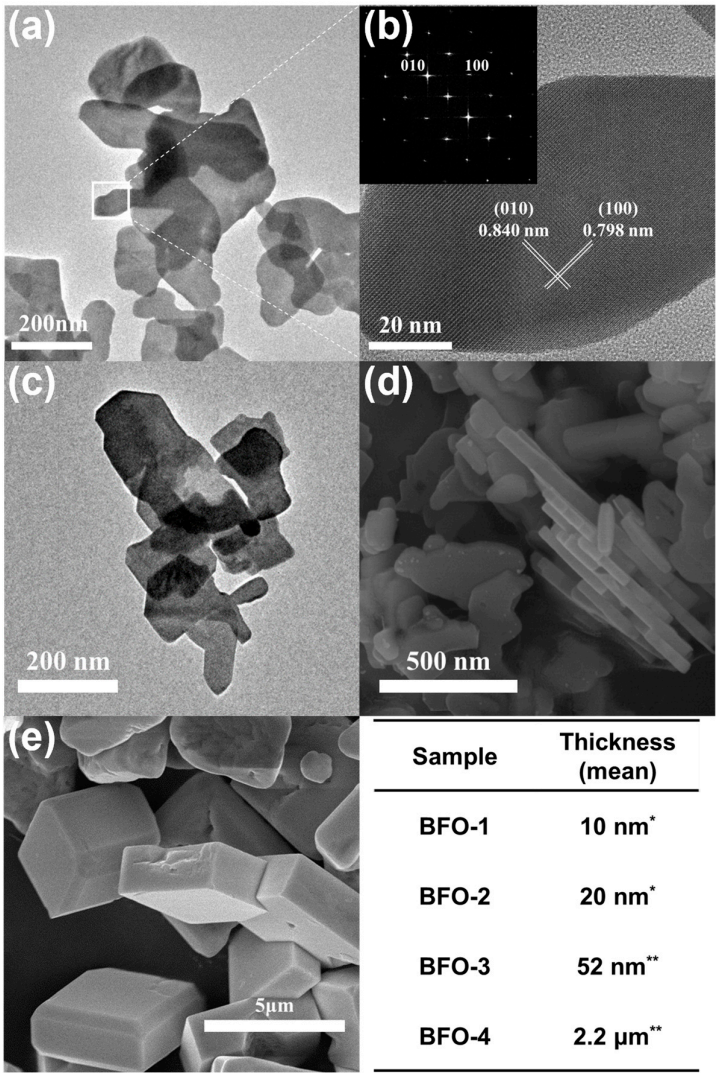

Sample	Thickness (mean)
BFO-1	10 nm*
BFO-2	20 nm*
BFO-3	52 nm**
BFO-4	2.2 μm**

Figure 2. Electron micrograph of BFO. TEM (**a**) and corresponding area HRTEM (**b**) of BFO-1, marked with lattice spacing, the inserted was the electron diffraction pattern, TEM of BFO-2 (**c**), SEM of BFO-3 (**d**), and BFO-4 (**e**), thickness mean values of BFO samples statistically obtained from their AFM results (*) or SEM results (**).

TEM images (Figure 2a) revealed that BFO-1 exhibited an irregular two-dimensional nanosheet structure. The lattice fringe spacing, calculated to be approximately 0.798 nm and 0.840 nm, corresponded to the (100) and (010) planes of orthorhombic $Bi_2Fe_4O_9$.

Combined with the XRD results, this confirmed that the exposed crystal plane of BFO-1 was (001). From the TEM results, BFO-2 and BFO-1 exhibited similar nanosheet-like microstructures. Additionally, the mean thickness values of BFO samples were statistically determined from their AFM results for BFO-1 and BFO-2, and from their SEM results for BFO-3 and BFO-4 (Figure S2). The thicknesses of BFO-1 and BFO-2 were ca. 10 nm and ca. 20 nm (Figure S3). When the hydrothermal synthesis time was extended to 48 h, the nanosheet thickness significantly increased, and the thickness of BFO-3 increased to approximately 52 nm., as observed in the SEM image (Figure 2d). BFO-4, with the largest size under the same crystal phase, exhibited a block structure with a thickness of ca. 2.2 μm (Figure 2e). This morphology resulted from the ordered crystal arrangement and growth during the hydrothermal process. The TEM image (Figure S4) showed that $BiFeO_3$ and ZnO had regular square nanosheet and cubic structures, respectively.

2.2. Thickness-Dependent Piezoelectric Activity of BFO

To verify the piezoelectric properties of BFO materials, we designed an ultrasound-induced current response experiment. A conductivity meter was employed to monitor the in situ changes in solution conductivity during the ultrasound process, with BFO-1 serving as the sample. The ultrasound was applied intermittently for 60 s, followed by a 60 s pause in each cycle, which was repeated multiple times. As shown in Figure S5, the conductivity of the BFO-1 solution increased under ultrasonic irradiation. When the ultrasonic power was doubled, the conductivity increased at a faster rate. Furthermore, to quantitatively evaluate the piezo-catalytic ability of BFO materials with different morphologies, a reduction experiment with hexavalent chromium (Cr (VI)) was conducted. Cr (VI) is carcinogenic and mutagenic in nature [34]; it can be reduced to trivalent chromium (Cr (III)) with less toxicity, relatively insoluble in water, and low fluidity.

All the piezoelectric materials reached adsorption equilibrium before the ultrasonic catalytic reaction commenced, and their adsorption capacities were not significant (Cr (VI)) adsorption rate < 10%, Figure S6). Therefore, the removal of Cr (VI) was primarily attributed to the piezo reaction. The performance of BFO materials and $BiFeO_3$ is shown in Figure 3a. After 60 min, the Cr (VI) conversion rate in the BFO-1 solution was approximately 62%, while the conversion rates for BFO-2, BFO-3, and BFO-4 were 60%, 20%, and less than 1%, respectively. As the thickness of the BFO material increased, catalytic efficiency decreased significantly. For BFO-4, with a thickness of 3 μm, the piezoelectric effect nearly disappeared (the "Only US" sample was subjected to ultrasound irradiation without any catalyst.). Research suggests that the piezoelectric properties exhibited by BFO nanoplates with a centrosymmetric crystal structure may stem from the presence of local dipoles on the exposed surfaces, which induce surface polarization [28]. These dipoles originate from distorted non-centrosymmetric ligands in the unit cell. This mechanism is not evident in bulk materials but becomes effective in nanomaterials, triggering piezoelectric catalytic reactions. Our experimental results are consistent with this observation, as the piezoelectric reduction of Cr (VI) gradually diminishes as the thickness of BFO materials increases from the nanoscale to the microscale. Additionally, carrier migration efficiency is higher in thinner materials. The time required for charge carriers to migrate to the surface is described by the following equation [35,36]:

$$\tau = r^2/(\pi^2 \times D) \quad (1)$$

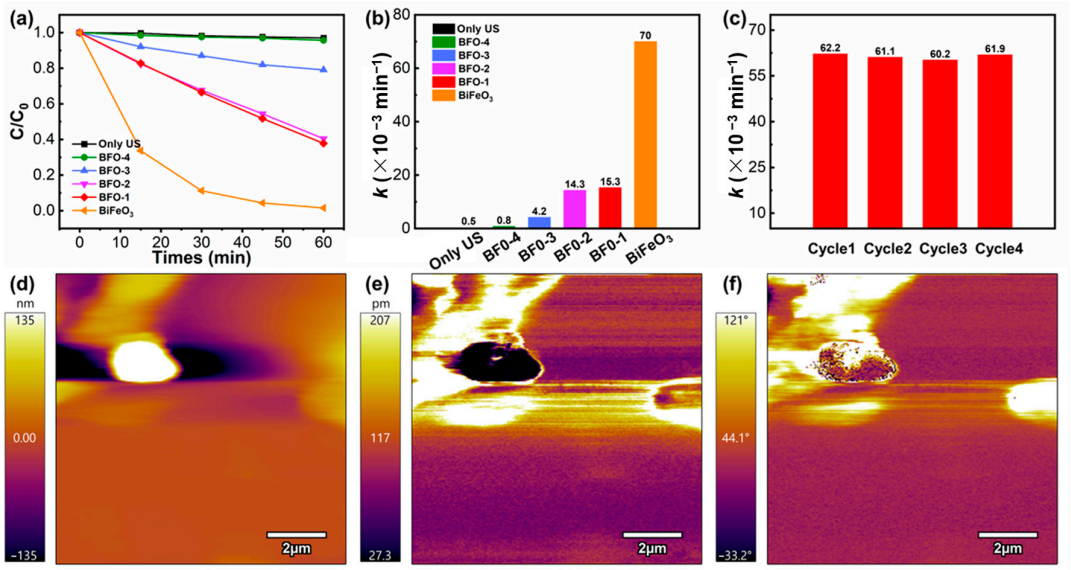

Figure 3. Piezocatalytic reduction of Cr (VI) process (**a**), chemical reaction rate constants of different materials, while nano-ZnO was not used because it is unstable under the experimental conditions (pH = 2.0, 40 kHz, 300 W). (**b**) and cycle stability experiment of BFO-1 (**c**); height mode (**d**), amplitude mode (**e**), and phase mode (**f**) of PFM diagram of BFO-1. Experiment conditions: Conducted in the darkness, [Cat] = 1 g/L, [Cr] 0 = 10 mg/L, pH = 2, the apparent rate constants were all obtained by the first-order kinetic model fitting for the average kinetic data, and the goodness of fit (R^2) was at least 0.99.

Where τ is the average diffusion time of charge carriers from inside to surface, *r* is the grain radius of the crystal, and *D* is the diffusion coefficient of the carrier. As the material size increases, the time for electrons to diffuse to the surface also increases, leading to more recombination of electrons and holes, which weakens the reduction ability. Figure 3b shows the apparent rate constants for the first-order kinetic reaction fitted to the Cr (VI) reduction curve. Further, we recovered BFO-1 through a simple filtration method and conducted a multi-cycle heavy metal ion reduction experiment, proving that BFO-1 maintained good catalytic activity (Figure 3c). In comparison, $BiFeO_3$ demonstrated better reduction performance than BFO materials due to its R3c space group. Although $BiFeO_3$ outperforms BFO in reducing Cr (VI), it is less effective in degrading emerging organic pollutants in aqueous solutions due to its unsuitable energy band position for generating oxidative active species, which will be discussed later.

The piezoelectric property of BFO-1 can also be supported by the results of its PFM experiment. The height mode of PFM images of the BFO-1, as shown in Figure 3d, exhibits a nanosheet structure, and the corresponding amplitude and phase modes of PFM (Figure 3e,f) exhibited a clear contrast, revealing the directions and strengths of piezoelectric polarization, as well as the piezoelectric performance of BFO-1 [37]. This suggests that the BFO nanosheet materials might primarily catalyze reactions through their piezoelectric processes under ultrasound, rather than through photocatalytic activation induced by sonoluminescence, even though BFO is a class of effective photocatalysts [25].

2.3. Enhanced Piezoelectric Activity of BFO Nanosheets Through Gold Loading

It is well established that noble metal nanoparticles are often deposited on the surface of photocatalysts to suppress the recombination of electron-hole pairs and promote carrier migration by modifying excitation mechanisms and energy transfer pathways [38,39]. Many piezoelectric materials also possess photocatalytic properties, and several studies

have demonstrated that noble metal decoration can enhance the efficiency of piezoelectric catalysis [7,40]. Furthermore, Lin et al. reported an effective approach to enhancing the piezocatalytic performance of $BaTiO_3$ through surface modification with Ag nanoparticles [41], attributing this improvement to the ability of Ag nanoparticles to efficiently capture free electrons.

BFO-1 exhibited the ability to generate piezoelectric electrons and reduce substances. Therefore, the aurochloric acid was introduced into the BFO-1 suspension under ultrasonic irradiation to synthesize gold nanodots-loaded bismuth ferrite composites, denoted as BFO@Au (Figure 1a). The XRD patterns of BFO@Au were identical to those of BFO-1 (Figure S8a), indicating no phase transition or chemical change in the BFO-1 component during ultrasonication. Due to the low content and poor crystallinity of Au, no distinct diffraction peaks were observed. The characteristic XPS peaks of Au^0 appeared at 83.4 eV and 86.9 eV (Figure S8c), confirming the presence of Au^0 in BFO@Au. To further investigate the chemical composition and elemental distribution of BFO@Au, TEM, and EDS mapping were performed. As shown in Figure 4, the elements Bi, Fe, and O were uniformly distributed in the BFO@Au, and Au nanodots, approximately 10 nm in size, were located at the edges of the nanoparticles. As presented in Table S1, the EDS quantitative results revealed that the atomic ratio of Bi, Fe, and O is close to 2:4:9, with approximately 0.24 Wt% gold loaded on the surface of BFO@Au. Notably, the selective deposition of Au provided further evidence supporting the piezoelectric effect of BFO-1, reflecting the directional migration of charge carriers, with ultrasonic-induced piezoelectric polarization occurring along the BFO-1 plane [37].

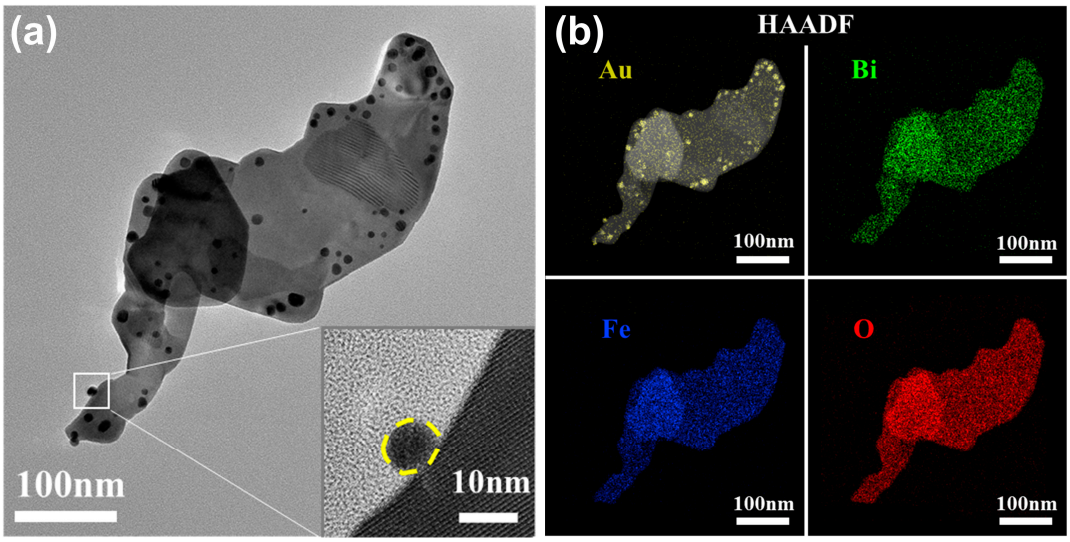

Figure 4. (**a**) HRTEM and EDS mapping of BFO@Au, (**b**) the inserted picture showed the outline of loaded gold nanodots with yellow dotted lines.

As predicted, the piezoelectric catalytic activity of BFO@Au was significantly higher than that of BFO-1, with a Cr (VI) reduction rate exceeding 70% within 60 min. This enhancement is likely due to the fact that the deposition of Au nanoparticles on the BFO surface facilitates the transfer of conduction band electrons from BFO to Au, thereby reducing the recombination of electron-hole pairs. However, with the increase in the gold precursor amount, the Cr (VI) reduction efficiency of the resulting Au and BFO-1 composite decreased (Figure S9), with BFO@Au (5 μmol) exhibiting nearly the same piezoelectric catalytic performance as BFO-1. A possible explanation is that variations in the gold precursor concentration often lead to changes in the gold loading and size in the product, which might in turn affect the electron concentration ability of the gold particles [42].

2.4. Piezocatalytic Degradation of APAP in Water

$Bi_2Fe_4O_9$ has been reported as a photocatalyst to remove pollutants for many years [43–45]. However, to the best of our knowledge, there are no reports on its use as a Fenton-like piezocatalyst for the degradation of organic pollutants. BFO-1 and BFO@Au can induce an in situ piezoelectric Fenton-like reaction due to the abnormal piezoelectric effect and the presence of iron. To evaluate their piezocatalytic activity, acetaminophen (APAP), a widely used medication, was chosen as a model pollutant.

All samples were immersed in the APAP solution for 30 min prior to ultrasonic irradiation to eliminate any potential adsorption of APAP (as shown in Figure S10). As shown in Figure 5a, BFO@Au exhibited the highest catalytic activity, with an APAP removal rate of approximately 90% in 30 min. BFO-1 achieved an APAP removal rate of 78%, outperforming nano-ZnO (45%), BFO-4 (35%), and $BiFeO_3$ (10%). The catalytic activity trend for the BFO series materials was consistent with previous results, which can be attributed to the generation and utilization of piezoelectric electrons. However, despite its strong Cr (VI) reduction ability, $BiFeO_3$ showed minimal degradation of APAP under ultrasonic conditions, as evidenced more clearly in the apparent reaction rate constant in Figure 5b.

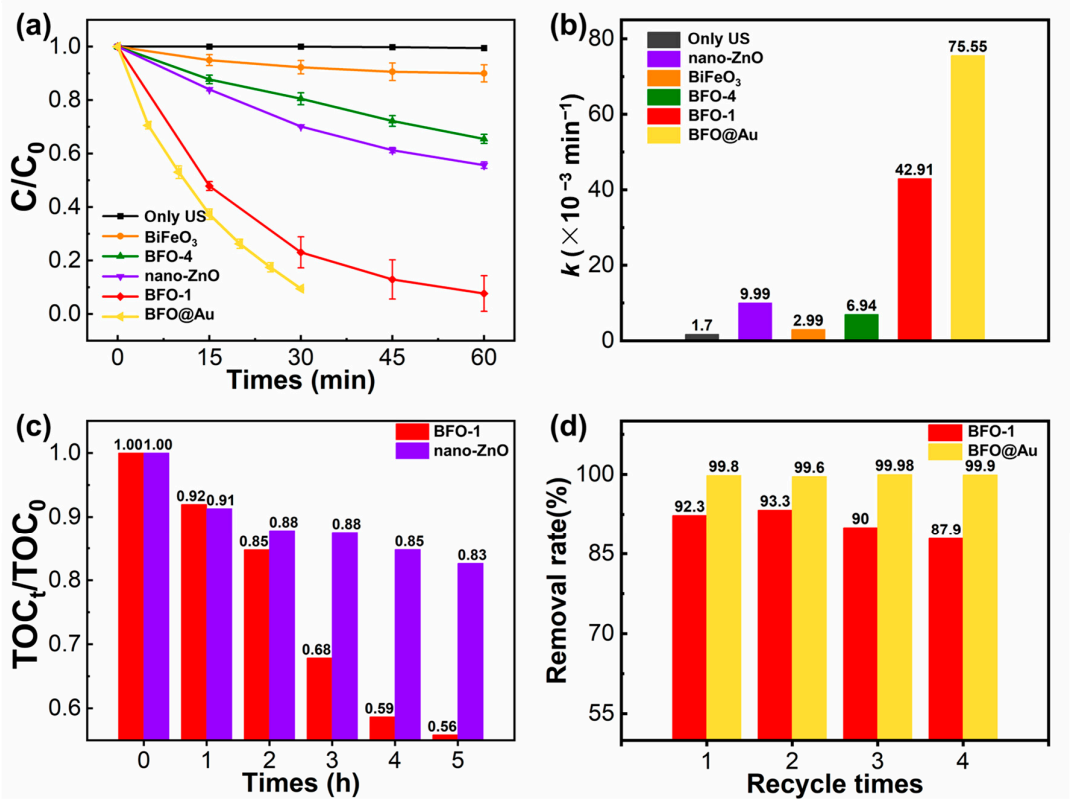

Figure 5. Piezocatalytic removal of APAP (**a**,**b**) and chemical reaction rate constants (**b**) of different materials, mineralization rate of APAP removal (**c**), cycle stability experiment of BFO-1 and BFO@Au (**d**).

Additionally, the mineralization rate of APAP was investigated by monitoring the total organic content (TOC) in the degradation system. The results in Figure 5c indicate that BFO-1 exhibited significantly better mineralization performance than commercial nano-ZnO. Moreover, BFO-1 and BFO@Au maintained good catalytic performance over four cycles (Figure 5d). In conclusion, we have demonstrated that BFO has the potential to be developed as a novel piezocatalyst for degrading organic pollutants in water.

2.5. Piezo-Fenton Mechanism over BFO

Spin-trapping EPR analyses were employed to elucidate the ROS generated in the BFO/ultrasound and $BiFeO_3$/ultrasound catalysis systems. We focused on $BiFeO_3$ from the perspective of active species because it had the best removal performance in Cr (VI) but the poorest APAP degradation. TEMPO was used as an electron spin-trapping agent, and the intensity decreases in the triple-peaks signal indicated the production of piezoelectric electrons. As shown in Figure 6a, after ultrasound for 10 min, the signal intensity of BFO-1 and $BiFeO_3$ was significantly weakened, confirming the electron generation ability of both materials. DMPO/DMSO and DMPO/H_2O were used as spin-trapping agents for superoxide anion and hydroxyl radical, respectively (Figures 6b,c). The signals of·O_2^- and ·OH increased significantly in the BFO-1 system, while no corresponding signal was detected in the $BiFeO_3$ system. We further quantified the concentration of H_2O_2 generated with different catalysts under various gas atmospheres (Figure 6d).

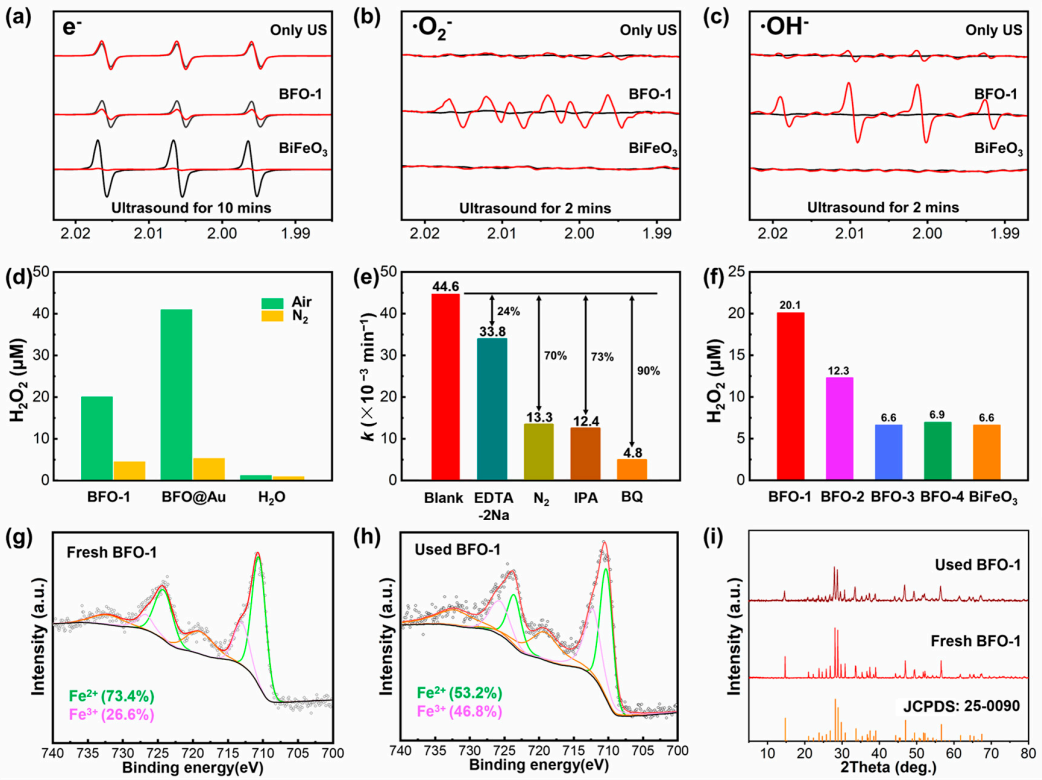

Figure 6. The EPR spin-trapping signals of BFO-1 and $BiFeO_3$ of e^- (**a**), O^{2-} (**b**), and ·OH (**c**) under ultrasound irradiation. The content of H_2O_2 in the solution after 30 min of ultrasonic irradiation (**d**) and (**f**), chemical reaction rate constant of BFO-1 in APAP removal with different quenchers or N_2 purging under ultrasonic irradiation, where 'Blank' denotes the reaction system without any quencher or N_2 (**e**), High-resolution XPS spectra of Fe2p of fresh BFO-1 (**g**), used BFO-1 (**h**), and XRD patterns (**i**).

The H_2O_2 concentration of BFO-1 was approximately 20 μM in the air atmosphere, which was higher than 4 μM in N_2 atmosphere. Additionally, BFO@Au exhibited a stronger ability to produce H_2O_2, reaching about 40 μM in the air atmosphere. These results indicated that H_2O_2 in the ultrasound-driven system was primarily generated through the reduction of oxygen molecules dissolved [46]. It is also worth noting that the H_2O_2 produced by BFO-1 undergoes rapid degradation through a Fenton-like reaction. Therefore, the results from the BFO-1 system reflect only the equilibrium concentration of

H_2O_2 in the coupled reaction. Based on these findings, we propose a ROS generation mechanism that involves both the piezoelectric effect and the band structure of semiconductor materials.

$$Bi_2Fe_4O_9+Ultrasonic \xrightarrow{Piezoelectric\ response} h^+ + e^- \quad (2)$$

$$e^- + O_2 \rightarrow \cdot O_2^- \quad (3)$$

$$O_2^- + e^- + 2H^+ \rightarrow H_2O_2 \quad (4)$$

$$Bi_2Fe_4O_9(Fe^{3+}) + e^- \rightarrow Bi_2Fe_4O_9(Fe^{2+}) \quad (5)$$

$$Bi_2Fe_4O_9(Fe^{2+}) + H_2O_2 \rightarrow Bi_2Fe_4O_9(Fe^{3+}) + \cdot OH + OH^- \quad (6)$$

$$\cdot OH + APAP \rightarrow H_2O + CO_2 \quad (7)$$

Under ultrasound irradiation, a polarized electric field is generated within the BFO-1 along the plane of the nanosheet. This polarization electric field leads to the separation of electron-hole pairs in BFO-1 Equation (2). On the one hand, the electrons on the surface of BFO combine with O_2 in the solution to generate O_2^- Equation (3). The $\cdot O_2^-$ then reacts with e^- and H^+ to produce H_2O_2 Equation (4), which undergoes a Fenton-like reaction in situ on the surface of BFO-1, generating a large amount of ·OH Equation (6). The·OH with strong oxidative capacity significantly oxidizes APAP to H_2O and CO_2, thereby increasing the mineralization rate under ultrasonic irradiation Equation (7). It is worth noting that the conversion of Fe^{3+} to Fe^{2+} is the rate-controlling step in the Fenton reaction [47]. In many previous studies on photo-Fenton reactions, researchers utilized photo-generated electrons or superoxide anion radicals to facilitate the process [48]. Here, a novel system is presented that combines piezo-generated electrons with Fenton-like catalysis, achieving advanced oxidation of pollutants with self-supplied H_2O_2 (Figure 7). Conversely, insufficient H_2O_2 is produced in the $BiFeO_3$/ultrasound system, preventing the initiation of the Fenton process, where H_2O_2 decomposes into·OH, leading to poor performance in the degradation of APAP.

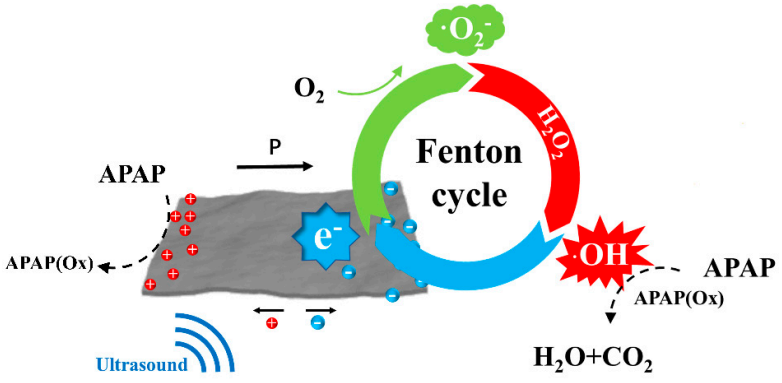

Figure 7. The mechanism diagram of the constructed system.

To further elucidate the role of reactive oxygen species (ROS) in the piezo-catalytic degradation of acetaminophen (APAP), the piezo-catalytic activity of BFO-1 was assessed using EDTA-2Na, isopropanol (IPA), and benzoquinone (BQ) as scavengers for holes, $\cdot O_2^-$, and ·OH, respectively (Figure 6e). The introduction of the hole scavenger led to a reduction in the reaction rate by approximately 24%, highlighting the involvement of holes in the degradation process. The valence band of BFO-1 is 1.13 eV more positive than the

potential of E (APAP/APAP) = 0.707 V (vs. NHE), allowing holes generated by the piezoelectric effect to oxidize APAP into its dimer form. While the piezoelectric hole oxidation contributes to the removal of APAP, it does not facilitate its mineralization. The inhibition of APAP degradation by $\cdot O_2^-$ and ·OH was approximately 72% and 89%, respectively, indicating that both species are essential for the reaction. Specifically, ·OH is derived from $\cdot O_2^-$, as previously discussed. As previously mentioned, it was found that purging the solution with N_2 to remove dissolved oxygen significantly reduced the concentration of H_2O_2 generated from the piezoelectric activation of molecular oxygen. As a result, the catalytic activity of BFO-1 in removing APAP was greatly reduced, showing a 70% decrease compared to the activity observed under conditions without N_2 purging. This suggests that in this Fenton catalytic system with self-supplied H_2O_2, the equilibrium concentration of H_2O_2 generated within the system is crucial for its Fenton catalytic ability. Furthermore, the $BiFeO_3$ system also generates a certain amount of H_2O_2 (Figure 6f); however, EPR results indicate that its production does not originate from $\cdot O_2^-$, and no OH is produced. This suggests that the $BiFeO_3$ system does not form a Fenton catalytic cycle, which may be related to the reactivity between iron species in $BiFeO_3$ and H_2O_2, and thus, H_2O_2 in this system accumulates to a certain extent.

The oxidation-reduction cycling of iron between different valence states is another key factor influencing the Fenton reaction. XPS analysis of BFO-1 was performed before and after the catalytic reaction, focusing on the changes in the valence states of iron species on the material's surface. It was observed that the ratio of Fe^{3+} to Fe^{2+} increased on the surface of used BFO-1 (Figure 6g and 6h). This could be attributed to two main factors: firstly, the piezoelectric process induces the generation of free electrons and more Fe^{3+} sites in $Bi_2Fe_4O_4$, and as previously described, these electrons react with O_2 to form $\cdot O_2^-$, which subsequently converts into hydrogen H_2O_2; secondly, Fe^{2+} participates in the decomposition of hydrogen peroxide, generating Fe^{3+} Equation (6). Additionally, it is important to note that the crystal phase composition of BFO-1 did not change before and after the catalytic reactions (Figure 6i), indicating that the conversion cycle between Fe^{3+} and Fe^{2+} occurred during the overall process. The most probable pathway for this transformation is the capture of piezoelectric electrons by Fe^{3+} Equation (5), which has been observed in many studies of piezoelectric catalysts containing iron [21,26]. These reactions occur simultaneously and cyclically during the piezoelectric-Fenton catalysis process, thereby facilitating the redox cycling of iron on the surface of BFO-1.

To further elucidate the differences in the piezoelectric processes of BFO and $BiFeO_3$, we conducted a study on the energy band structures of these materials. All samples exhibited similar photoabsorption characteristics across the UV to the visible light spectrum. Two absorption edges appeared at approximately 610 nm and 800 nm, consistent with previously reported data [49]. The absorption between 610 nm and 800 nm was attributed to the d–d transitions of Fe^{3+}, resulting from the energy splitting of the Fe 3d orbital [28].The bandgap (E_g) of materials were measured using UV-Vis DRS and estimated by Tauc formula Equation (8):

$$\alpha h\nu = A\left(h\nu - E_g\right)^{n/2} \quad (8)$$

where α is the absorption coefficient, $h\nu$ equal to the energy of photoelectrons, A is a constant, Eg is the band gap energy, respectively, and n = 1 for direct band gap semiconductors. The Kubelka Munk (K-M) plots describe the relationship between E_g and $(\alpha Eg)^2$ converted from the Tauc formula (Figure 8a). The valence band (E_{VB}) position of the material was measured by the XPS valence band spectrum (Figure 8b), and the conduction band (E_{CB}) position was calculated in combination with the bandgap (Table 1).

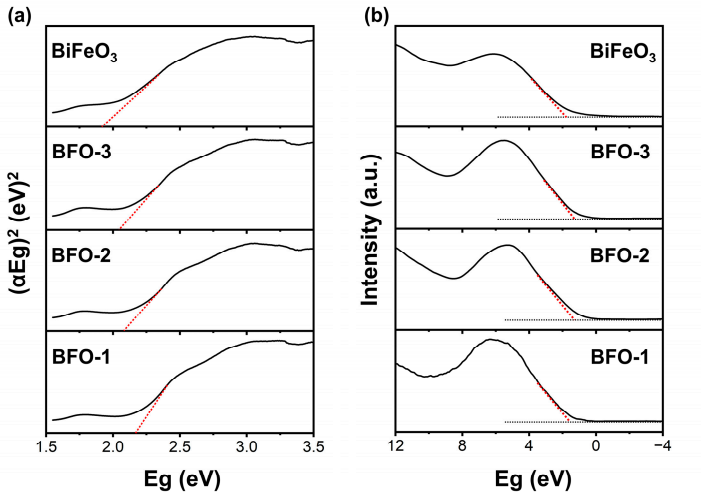

Figure 8. (**a**) K-M plots for the band gap estimation and (**b**) XPS valence band spectrum of BFOs.

Table 1. Eg, EVB, and ECB (vs. RHE) of various BFO NPs calculated on the basis of UV-vis DRS and XPS valence band spectra.

	BFO-1	**BFO-2**	**BFO-3**	**$BiFeO_3$**
E_g	2.18	2.13	2.04	1.89
E_{VB}	1.42	1.4	1.32	1.63
E_{CB}	−0.76	−0.73	−0.72	−0.26

For BFO-1, BFO-2, and BFO-3, as their thickness gradually increases, their band gap width decreases from 2.18 eV to 2.04 eV. The BFO had a more negative conduction band than $E(O_2/\cdot O_2^-) = -0.33$ V, which could convert O_2 into O_2^-, once piezoelectric electrons are generated. The degree of nanostructuring (thickness) imparts varying piezoelectric activity to BFO. However, the conduction and valence bands of prepared $BiFeO_3$ were −0.26 eV and 1.63 eV (vs. NHE, Figure 8), respectively. Its conduction band is more positive than $E(O_2/\cdot O_2^-) = -0.33$ V; O_2 in the solution could not be converted to $\cdot O_2^-$ effectively, resulting in a limited production of H_2O_2, while the valence band is more negative than $E(H_2O/OH) = 2.72$ V, indicating that $BiFeO_3$ could not produce OH by oxidizing H_2O directly, too. On the other hand, the conduction band of BFO is about 0.5 V lower than that of $BiFeO_3$, which gives its conduction band electrons a stronger reducing ability. This explains why the piezoelectric electrons of BFO can effectively participate in the Fenton reaction and reduce ferric iron.

3. Materials and Methods

3.1. Materials

Bismuth nitrate ($Bi(NO_3)_3{\cdot}5H_2O$), ferric nitrate ($Fe(NO_3)_3{\cdot}9H_2O$), Diphenylcarbazide ($C_{13}H_{14}N_4O$), and horseradish catalase were purchased from Sinopharm Chemical Reagent Ltd. (Shanghai, China). *N*-Acetyl-p-aminophenol (APAP), Chlorauric acid ($H[AuCl_4]{\cdot}3H_2O$, ≥99%), 2,2,6,6-Tetramethylpiperidine (TEMP, $C_9H_{19}N$, ≥98%), 2,2,6,6-Tetramethylpiperidine-1-oxyl (free radical) (TEMPO, $C_9H_{18}NO$, ≥98%), and 5,5-Dimethyl-1-pyrroline *N*-oxide (DMPO, $C_6H_{11}NO$, ≥97%) were purchased from Aladdin Ltd. (Shanghai, China). All chemicals used in this study were analytical grade without any pretreatment if not specifically mentioned.

3.2. Synthesis of $Bi_2Fe_4O_9$ (BFO-n, n = 1~4) and $BiFeO_3$

A series of $Bi_2Fe_4O_9$ nanosheets (BFOs) with different thicknesses were synthesized by the slightly modified hydrothermal method referred to previous report [29]. The thickness of BFOs gradually increases from nano-sheet (BFO-1) to bulk (BFO-4).

BFO-1: 2.5 mmol of $Bi(NO_3)\cdot 5H_2O$ and 2.5 mmol of $Fe(NO_3)_3\cdot 9H_2O$ (with a 1:1 molar ratio) were dissolved in 4 mL of 1 M HNO_3; 2 ml of concentrated nitric acid (68–70%) was added to the solution under vigorous stirring for 30 min. A total of 30 mL of 10 M KOH was added, stirring for another 30 min. Then, the mixture was transferred to a stainless-steel autoclave with a Teflon liner and kept at 200 °C for 24 h. The obtained product was washed with deionized water and ethanol and dried at 80 °C overnight.

BFO-2: Using a similar synthetic method to BFO-1, the amount of concentrated nitric acid was reduced to 1 mL, and the remaining hydrothermal conditions remained unchanged.

BFO-3: Using a similar synthetic method to BFO-1, the heating time of the hydrothermal reaction was extended to 48 h with the remaining reaction conditions unchanged.

BFO-4: 1 mmol of $Bi(NO_3)_3\cdot 5H_2O$ and 2 mmol of $Fe(NO_3)_3\cdot 9H_2O$ (with a 1:2 molar ratio) were added to deionized water; 0.32 mol of KOH was added to the solution. A hydrothermal treatment was conducted on the above solution at 160 °C for 12 h. The final products were collected by centrifugation, rinsed with distilled water and ethanol, and dried at 70 °C for 4 h before further characterization.

$BiFeO_3$ was synthesized by a hydrothermal method, 5 mmol $Bi(NO_3)_3\cdot 5H_2O$ and 5 mmol $Fe(NO_3)_3\cdot 9H_2O$ (with a 1:1 molar ratio) were dissolved in 5 mL 1 M HNO_3 by agitation in a beaker, and then 32 mL 10 M KOH was added and form a red precipitate, after stirring for 45 min, the mixture transferred to a high-pressure hydrothermal reactor to react at 180 °C for 24 h, and then cooled to room temperature naturally. The obtained products were washed with deionized water and ethanol and collected after drying.

3.3. Synthesis of BFO@Au

The synthesis of BFO@Au is assisted by the ultrasound method. A total of 50 mg BFO-1 was dissolved in 49 mL deionized water, added with 1 mL methanol and 10 uL 0.1 M chloroauric acid (1 μmol). It should be noted that methanol, at a volume ratio of 2%, was introduced into the solution. Under the experimental conditions, methanol did not directly reduce chloroauric acid to gold. A control experiment was conducted in which BFO-1 was omitted, with all other conditions remaining unchanged, and no significant gold formation was observed. The role of methanol was to react with the holes generated in BFO-1 under ultrasonic excitation, thereby ensuring that piezoelectric electrons could more effectively reduce chloroauric acid. The homogeneous solution was sonicated in the dark for 30 min. The obtained solid was washed with deionized water and ethanol. In addition, by varying the amount of chloroauric acid (2.5 and 5 μmol), the corresponding products are obtained as BFO@Au (2.5 μmol) and BFO@Au (5 μmol), respectively. It should be noted that BFO@Au only refers to BFO@Au (1 μmol), which denotes the product obtained by adding 1 micromole of chloroauric acid into the BFO-1 suspension during the reaction unless otherwise specified.

3.4. Characterization

X-ray diffraction (XRD) patterns of samples were recorded using a D8 Advance diffractometer (Bruker Inc., Germany) equipped with Cu Kα radiation. Scanning electron microscope (SEM) images were obtained using a LEO 1430VP scanning electron microscope at an accelerating voltage of 20 kV. A high-resolution transmission electron microscopy (HRTEM) image was obtained using a TALOS F200 field emission high-resolution transmission electron microscopy at an accelerating voltage of 200 kV.

The high-resolution transmission electron microscopy (HRTEM) images were obtained using a TALOS F200 S/TEM (Thermo Fisher Scientific, Waltham, United States) at an accelerating voltage of 200 kV. X-ray photoelectron spectroscopy (XPS) measurements were carried out using a Thermo ESCALAB 250xi apparatus. APAP removal intermediates were detected using an Agilent 1200 HPLC (Agilent Technologies, Santa Clara, United States) with a UV detector set at 250 nm. Electronic and reactive oxygen species (ROS), like ·OH and $\cdot O_2^-$, were detected by a Bruker MiniScope MS5000 EPR (Bruker Corporation, Billerica, United States.). The piezoresponse force microscopy (PFM) was measured by MFP-3D Origin (Oxford Instruments Technology, Shanghai, China in vector PFM mode. The ultrasonic radiation was provided by the Kunshan numerical control ultrasonic wave washing machine (KQ-300 DE, Kunshan Ultrasonic Instruments Co., Ltd., Kunshan, China).

The generation of e^-, O_2^-, or OH was detected via EPR using a MiniScope MS-5000 spectrometer (Magnettech GmbH, Berlin, Germany) with 50 mM TEMPO in water, 50 mM DMPO in methanol, or 50 mM DMPO in water as the radical spin-trapped reagents under ultrasonic irradiation.

3.5. Piezoelectric Activity

All experiments were conducted at 20.0 °C in dark environments to avoid the possible effects of heat and light. A total of 50 mg of piezo-catalyst was dispersed into 50 mL of solution containing APAP (50 mM) or Cr (VI) (pH = 2.0 potassium dichromate solution, 10 mg/L) and stirred gently for 30 min to ensure adsorption-desorption equilibrium. The resulting suspension was put into a glass flask and then transferred into an ultrasonic cleaner (KQ-300DE, Kunshan Ultrasonic Instruments Co., Ltd., Kunshan, China), which was equipped with a circulation water-cooling pipe to control temperature. The reactions were carried out under 40 kHz, 300 W ultrasound, and the position of the flask in the ultrasonic cleaner was kept unchanged for all trials, unless stated otherwise. The reaction suspension was sampled at regular time intervals and then centrifuged for subsequent concentration tests. The content of Cr (VI) was determined by the color rendering method [50]. The concentration of APAP was detected in the supernatant by an Agilent 1200 HPLC (Agilent Technologies, Santa Clara, United States). When investigating the degradation kinetics of APAP by the materials under ultrasonic treatment, samples were generally taken every 15 min to monitor the change in APAP concentration over a 1 h period. However, for BFO@Au, it was observed that APAP was completely degraded after 45 min. To obtain a more accurate rate constant, the sampling interval was reduced to 5 min, and the change in APAP concentration was monitored over a 30 min period. All experiments were repeated three times, and the average results were given. In the cyclic experiments, the catalyst was recovered by centrifugation, cleaned, and reused, with all other experimental conditions unchanged. To quench a certain ROS during reactions, TEOA, IPA, or p-BQ were added together with the catalyst and APAP into the reaction system as the quencher to h^+, OH, or O_2^-, respectively. In addition, the cumulative concentration of hydrogen peroxide produced during the reactions was determined by fluorometric analysis of the fluorescent dimer, which formed in the horseradish peroxidase-catalyzed reaction of hydrogen peroxide with 4-hydroxyphenylacetic acid.

4. Conclusions

Our study investigates the piezoelectric properties and applications of BFO nanosheets, confirming their significant piezoelectric effects, which can be modulated by controlling the thickness. A novel piezo-Fenton catalytic system based on BFO nanosheets was developed, where piezoelectric electrons generated during ultrasonic irradiation facilitate the in situ production of hydrogen peroxide (H_2O_2), a key element in the Fenton-

like reaction. The piezoelectric electrons directly or indirectly facilitate the redox cycling of iron in the Fenton process, thereby enhancing the overall catalytic efficiency. The system effectively degraded APAP, exhibiting strong oxidation capacity, stability, and recyclability. Reactive oxygen species generated during degradation were confirmed through electron paramagnetic resonance spectroscopy, revealing the mechanism of the piezo-Fenton reaction. Overall, BFO nanosheets demonstrate great potential as piezoelectric-driven Fenton systems, with their ability to self-supply H_2O_2 and accelerate the redox cycling of iron, offering a promising solution for wastewater treatment and other advanced oxidation processes across various fields.

Supplementary Materials: The following supporting information can be downloaded at: www.mdpi.com/xxx/s1, Figure S1: XRD patterns of the BiFeO3 and nano-ZnO; Figure S2: The thickness distribution and average value of BFO nanosheets. thickness mean values of BFO samples statistically obtained from their AFM results (BFO-1, BFO-2) or SEM results (BFO-3, BFO-4); Figure S3: AFM image of BFO-1(a) and the corresponding thickness at the red line (b); 2D (c) and 3D (d) AFM images of BFO-2; Figure S4: TEM image of ZnO (a) and $BiFeO_3$ (b); Figure S5: Ultrasonic-conductivity response experiment device (a) and the conductivity of BFO-1 solution increased with the ultrasonic irritated (b); Figure S6: The concentration change of Cr (VI) in the process of adsorption-desorption equilibrium with catalysis, all experiments were carried out at 20 °C in dark environment; Figure S7: Vertical and lateral PFM responses of BFO-1 across resonant frequency (a,b), Resonance peaks at different applied voltages and Linear correlation between drive voltage and piezoresponse (c); Figure S8: XRD patterns of BFO-1 and BFO@Au (a), XPS spectra of BFO-1 and BFO@Au (b) and corresponding fine peaks of Au 4f (c); Figure S9: The concentration change of Cr (VI) in the process of adsorption-desorption equilibrium with catalysis (a), piezocatalytic reduction rate of Cr (VI) (b) and the chemical reaction rate constants of different materials; Figure S10: The concentration change of APAP in the process of adsorption-desorption equilibrium with different catalysis; Table S1: EDS Quantitative Results on BFO materials

Author Contributions: Conceptualization, Z.Y.; methodology, C.Z., S.J., L.G., and W.L.; formal analysis, C.Z. and S.J.; investigation, S.J., L.G., H.Z., Y.Z., and W.L.; data curation, T.M. and N.Z.; writing—original draft preparation, C.Z., L.G., and W.L.; writing—review and editing, Z.Y. and S.J.; supervision, Z.Y.; project administration, Z.Y.; funding acquisition, C.Z. and Z.Y. All authors have read and agreed to the published version of the manuscript.

Funding: The research was financially supported by the Research Foundation from the Hubei Provincial Department of Water Resources (2022-218-006-001) and the Key Research Project from the Hubei Provincial Department of Water Resources (HBSLKY202402).

Institutional Review Board Statement: Not applicable.

Informed Consent Statement: Not applicable.

Data Availability Statement: The raw data supporting this article's conclusions will be made available by the authors of this article, and Supplementary data can be made available upon request.

Conflicts of Interest: The authors declare no conflicts of interest.

References

1. Li, Y.; Li, C.; Wang, Z.; Liu, Y.; Jia, Y.; Li, F.; Ren, R.; Ikhlaq, A.; Kumirska, J.; Siedlecka, E.M.; et al. Navigating the complexity of pharmaceutical wastewater treatment by "effective strategy, emerging technology, and sustainable solution". *J. Water Process Eng.* **2024**, *63*, 105404.
2. Igwegbe, C.A.; Aniagor, C.O.; Oba, S.N.; Yap, P.-S.; Iwuchukwu, F.U.; Liu, T.; de Souza, E.C.; Ighalo, J.O. Environmental protection by the adsorptive elimination of acetaminophen from water: A comprehensive review. *J. Ind. Eng. Chem.* **2021**, *104*, 117–135.
3. Phong Vo, H.N.; Le, G.K.; Hong Nguyen, T.M.; Bui, X.-T.; Nguyen, K.H.; Rene, E.R.; Vo, T.D.H.; Thanh Cao, N.-D.; Mohan, R. Acetaminophen micropollutant: Historical and current occurrences, toxicity, removal strategies and transformation pathways in different environments. *Chemosphere* **2019**, *236*, 124391.

4. Wu, J.L.; Liu, Z.H.; Ma, Q.G.; Dai, L.; Dang, Z. Occurrence, removal and risk evaluation of ibuprofen and acetaminophen in municipal wastewater treatment plants: A critical review. *Sci. Total Environ.* **2023**, *891*, 164600.
5. Samal, K.; Mahapatra, S.; Hibzur Ali, M. Pharmaceutical wastewater as Emerging Contaminants (EC): Treatment technologies, impact on environment and human health. *Energy Nexus* **2022**, *6*, 100076.
6. Liang, Z.; Yan, C.-F.; Rtimi, S.; Bandara, J. Piezoelectric materials for catalytic/photocatalytic removal of pollutants: Recent advances and outlook. *Appl. Catal. B Environ.* **2019**, *241*, 256–269.
7. Zheng, H.; Wang, Y.; Liu, J.; Wang, J.; Yan, K.; Zhu, K. Recent advancements in the use of novel piezoelectric materials for piezocatalytic and piezo-photocatalytic applications. *Appl. Catal. B Environ.* **2024**, *341*, 123335.
8. Tu, S.; Guo, Y.; Zhang, Y.; Hu, C.; Zhang, T.; Ma, T.; Huang, H. Piezocatalysis and Piezo-Photocatalysis: Catalysts Classification and Modification Strategy, Reaction Mechanism, and Practical Application. *Adv. Funct. Mater.* **2020**, *30*, 2005158.
9. Jin, X.; Li, X.; Dong, L.; Zhang, B.; Liu, D.; Hou, S.; Zhang, Y.; Zhang, F.-M.; Song, B. Enhancement and inhibition of photocatalytic hydrogen production by fine piezoelectric potential tuning over piezo-photocatalyst. *Nano Energy* **2024**, *123*, 109341.
10. Mushtaq, F.; Chen, X.; Hoop, M.; Torlakcik, H.; Pellicer, E.; Sort, J.; Gattinoni, C.; Nelson, B.J.; Pané, S. Piezoelectrically Enhanced Photocatalysis with $BiFeO_3$ Nanostructures for Efficient Water Remediation. *iScience* **2018**, *4*, 236–246.
11. Liu, S.; Jing, B.; Nie, C.; Ao, Z.; Duan, X.; Lai, B.; Shao, Y.; Wang, S.; An, T. Piezoelectric activation of peroxymonosulfate by MoS_2 nanoflowers for the enhanced degradation of aqueous organic pollutants. *Environ. Sci. Nano* **2021**, *8*, 784–794.
12. Le, K.T.; Pham, N.N.T.; Liao, Y.-S.; Ranjan, A.; Lin, H.-Y.; Chen, P.-H.; Nguyen, H.; Lu, M.Y.; Lee, S.G.; Wu, J.M. Piezoelectricity of strain-induced overall water splitting of $Ni(OH)_2/MoS_2$ heterostructure. *J. Mater. Chem. A* **2023**, *11*, 3481–3492.
13. Qian, W.; Yang, W.; Zhang, Y.; Bowen, C.R.; Yang, Y. Piezoelectric Materials for Controlling Electro-Chemical Processes. *Nano-Micro Lett.* **2020**, *12*, 149.
14. Harish, V.; Ansari, M.M.; Tewari, D.; Yadav, A.B.; Sharma, N.; Bawarig, S.; García-Betancourt, M.-L.; Karatutlu, A.; Bechelany, M.; Barhoum, A. Cutting-edge advances in tailoring size, shape, and functionality of nanoparticles and nanostructures: A review. *J. Taiwan Inst. Chem. Eng.* **2023**, *149*, 105010.
15. Chung, Y.-J.; Yang, C.-S.; Lee, J.-T.; Wu, G.H.; Wu, J.M. Coupling Effect of Piezo–Flexocatalytic Hydrogen Evolution with Hybrid 1T- and 2H-Phase Few-Layered $MoSe_2$ Nanosheets. *Adv. Energy Mater.* **2020**, *10*, 2002082.
16. Wu, M.-H.; Lee, J.-T.; Chung, Y.J.; Srinivaas, M.; Wu, J.-M. Ultrahigh efficient degradation activity of single- and few-layered $MoSe_2$ nanoflowers in dark by piezo-catalyst effect. *Nano Energy* **2017**, *40*, 369–375.
17. Nie, G.; Yao, Y.; Duan, X.; Xiao, L.; Wang, S. Advances of piezoelectric nanomaterials for applications in advanced oxidation technologies. *Curr. Opin. Chem. Eng.* **2021**, *33*, 100693.
18. Lan, S.; Jing, B.; Yu, C.; Yan, D.; Li, Z.; Ao, Z.; Zhu, M. Protrudent Iron Single-Atom Accelerated Interfacial Piezoelectric Polarization for Self-Powered Water Motion Triggered Fenton-Like Reaction. *Small* **2022**, *18*, 2105279.
19. Wang, P.; Li, X.; Fan, S.; Chen, X.; Qin, M.; Long, D.; Tadé, M.O.; Liu, S. Impact of oxygen vacancy occupancy on piezo-catalytic activity of $BaTiO_3$ nanobelt. *Appl. Catal. B Environ.* **2020**, *279*, 119340.
20. Chimupala, Y.; Phromma, C.; Yimklan, S.; Semakul, N.; Ruankham, P. Dye wastewater treatment enabled by piezo-enhanced photocatalysis of single-component ZnO nanoparticles. *RSC Adv.* **2020**, *10*, 28567–28575.
21. Ge, L.; Xiao, J.; Liu, W.; Ren, G.; Zhou, C.; Liu, J.; Zou, J.; Yang, Z. A Piezo-Fenton System with Rapid Iron Cycling and Hydrogen Peroxide Self-Supply Driven by Ultrasound. *Chem. Eur. J.* **2022**, *28*, e202202494.
22. Lv, W.; Kong, L.; Lan, S.; Feng, J.; Xiong, Y.; Tian, S. Enhancement effect in the piezoelectric degradation of organic pollutants by piezo-Fenton process. *J. Chem. Technol. Biotechnol.* **2017**, *92*, 152–156.
23. Wei, Y.; Zhang, Y.; Miao, J.; Geng, W.; Long, M. In-situ utilization of piezo-generated hydrogen peroxide for efficient p-chlorophenol degradation by Fe loading bismuth vanadate. *Appl. Surf. Sci.* **2021**, *543*, 148791.
24. Qian, W.; Zhao, K.; Zhang, D.; Bowen, C.R.; Wang, Y.; Yang, Y. Piezoelectric Material-Polymer Composite Porous Foam for Efficient Dye Degradation via the Piezo-Catalytic Effect. *ACS Appl. Mater. Interfaces* **2019**, *11*, 27862–27869.
25. Gao, W.; Tang, L.; Zhu, M.; Yuan, Y.; Guo, S.; Yin, S. Aggregation-based growth of faceted $Bi_2Fe_4O_9$ micro-cuboids with a remarkable visible light photo-Fenton catalytic activity. *CrystEngComm* **2024**, *26*, 1410–1417.
26. Su, C.; Li, C.; Li, R.; Wang, W. Insights into highly efficient piezocatalytic molecule oxygen activation over $Bi_2Fe_4O_9$: Active sites and mechanism. *Chem. Eng. J.* **2023**, *452*, 139300.
27. Su, C.; Li, R.; Li, C.; Wang, W. Piezo-promoted regeneration of Fe^{2+} boosts peroxydisulfate activation by $Bi_2Fe_4O_9$ nanosheets. *Appl. Catal. B Environ.* **2022**, *310*, 121330.
28. Du, Y.; Lu, T.; Li, X.; Liu, Y.; Sun, W.; Zhang, S.; Cheng, Z. High-efficient piezocatalytic hydrogen evolution by centrosymmetric $Bi_2Fe_4O_9$ nanoplates. *Nano Energy* **2022**, *104*, 107919.

29. Zhang, Q.; Gong, W.; Wang, J.; Ning, X.; Wang, Z.; Zhao, X.; Ren, W.; Zhang, Z. Size-dependent magnetic, photoabsorbing, and photocatalytic properties of single-crystalline $Bi_2Fe_4O_9$ semiconductor nanocrystals. *J. Phys. Chem. C* **2011**, *115*, 25241–25246.
30. Javed, R.; Zia, M.; Naz, S.; Aisida, S.O.; Ain, N.u.; Ao, Q. Role of capping agents in the application of nanoparticles in biomedicine and environmental remediation: Recent trends and future prospects. *J. Nanobiotechnology* **2020**, *18*, 172.
31. Lin, F.; Yu, Q.; Deng, L.; Zhang, Z.; He, X.; Liu, A.; Shi, W. Effect of La/Cr codoping on structural transformation, leakage, dielectric and magnetic properties of $BiFeO_3$ ceramics. *J. Mater. Sci.* **2017**, *52*, 7118–7129.
32. Chudasama, D.K.; Shrimali, V.G.; Vaishnani, A.; Panchasara, C.M.; Raval, N.; Jambukiya, U.; Amouri, A.; Dhruv, D.; Joshi, A.D.; Solanki, P.S.; et al. Investigation on structural, optical and electrical properties of $BiFeO_3$:ZnO nano–micro particles–matrix composite. *J. Alloys Compd.* **2023**, *960*, 170771.
33. Thakur, S.; Bhattacharya, R.; Neogi, S.; Neogi, S. Enhancement of microwave absorption properties of epoxy by sol–gel-Synthesised ZnO nanoparticles. *Indian Chem. Eng.* **2016**, *58*, 310–324.
34. Pratush, A.; Kumar, A.; Hu, Z. Adverse effect of heavy metals (As, Pb, Hg, and Cr) on health and their bioremediation strategies: A review. *Int. Microbiol.* **2018**, *21*, 97–106.
35. Liu, B.; Zhao, X.; Parkin, I.P.; Nataka, K. Charge carrier transfer in photocatalysis. *Interface Sci. Technol.* **2020**, *31*, 103–159.
36. Graetzel, M.; Frank, A.J. Interfacial electron-transfer reactions in colloidal semiconductor dispersions. Kinetic analysis. *J. Phys. Chem.* **1982**, *86*, 2964–2967.
37. Wang, K.; Shao, D.; Zhang, L.; Zhou, Y.; Wang, H.; Wang, W. Efficient piezo-catalytic hydrogen peroxide production from water and oxygen over graphitic carbon nitride. *J. Mater. Chem. A* **2019**, *7*, 20383–20389.
38. Xiang, D.; Liu, Z.; Wu, M.; Liu, H.; Zhang, X.; Wang, Z.; Wang, Z.L.; Li, L. Enhanced Piezo-Photoelectric Catalysis with Oriented Carrier Migration in Asymmetric Au-ZnO Nanorod Array. *Small* **2020**, *16*, e1907603.
39. Zhang, Z.; Zhang, C.; Zheng, H.; Xu, H. Plasmon-Driven Catalysis on Molecules and Nanomaterials. *Acc. Chem. Res.* **2019**, *52*, 2506–2515.
40. Liu, Y.-f.; Guo, R.-t.; Guo, S.-h.; Yu, L.-q.; Yan, J.-s.; Pan, W.-g. Recent progress of piezoelectric materials applied in photocatalytic CO_2 reduction: A review. *J. Environ. Chem. Eng.* **2024**, *12*, 114782.
41. Lin, E.; Wu, J.; Qin, N.; Yuan, B.; Bao, D. Silver modified barium titanate as a highly efficient piezocatalyst. *Catal. Sci. Technol.* **2018**, *8*, 4788–4796.
42. Murdoch, M.; Waterhouse, G.; Nadeem, M.; Metson, J.; Keane, M.; Howe, R.; Llorca, J.; Idriss, H. The effect of gold loading and particle size on photocatalytic hydrogen production from ethanol over Au/TiO_2 nanoparticles. *Nat. Chem.* **2011**, *3*, 489–492.
43. Chen, W.; Xing, Z.; Zhang, N.; Cheng, T.; Ren, B.; Liu, X.; Wang, Z.; Li, Z.; Zhou, W. Hierarchical $Bi_2Fe_4O_9$/BiOI S-scheme heterojunctions with exceptional hydraulic shear induced photo-piezoelectric catalytic activity. *Npj Clean Water* **2024**, *7*, 86.
44. Wu, C.; Xing, Z.; Wang, Y.; Peng, H.; Kong, W.; Yang, S.; Li, Z.; Zhou, W. $Bi_2Fe_4O_9$@$ZnIn_2S_4$ S-scheme laminated heterojunction photocatalyst towards optimized photocatalytic performance. *Dalton Trans.* **2023**, *52*, 7724–7730.
45. Shah, J.H.; Huaqian, Z.; Mehmood, R.; Channa, A.I.; Kazmi, J.; Zhang, L.; Rosei, F.; Wang, Z. Enhanced photocatalytic activity in Mn-doped multiferroic $BiFeO_3$. *J. Mater. Chem. A* **2024**, *12*, 11644–11655.
46. Wang, K.; Xu, X.; Lu, L.; Li, A.; Han, X.; Wu, Y.; Miao, J.; Jiang, Y. Magnetically recoverable Ag/$Bi_2Fe_4O_9$ nanoparticles as a visible-light-driven photocatalyst. *Chem. Phys. Lett.* **2019**, *715*, 129–133.
47. Wang, J.; Xie, T.; Liu, X.; Wu, D.; Li, Y.; Wang, Z.; Fan, X.; Zhang, F.; Peng, W. Enhanced redox cycle of Fe^{3+}/Fe^{2+} on Fe@NC by boron: Fast electron transfer and long-term stability for Fenton-like reaction. *J. Hazard. Mater.* **2023**, *445*, 130605.
48. Qin, L.; Wang, Z.; Fu, Y.; Lai, C.; Liu, X.; Li, B.; Liu, S.; Yi, H.; Li, L.; Zhang, M. Gold nanoparticles-modified $MnFe_2O_4$ with synergistic catalysis for photo-Fenton degradation of tetracycline under neutral pH. *J. Hazard. Mater.* **2021**, *414*, 125448.
49. Li, B.; Lai, C.; Zeng, G.; Qin, L.; Yi, H.; Huang, D.; Zhou, C.; Liu, X.; Cheng, M.; Xu, P.; et al. Facile Hydrothermal Synthesis of Z-Scheme $Bi_2Fe_4O_9$/Bi_2WO_6 Heterojunction Photocatalyst with Enhanced Visible Light Photocatalytic Activity. *ACS Appl. Mater. Interfaces* **2018**, *10*, 18824–18836.
50. Wang, Y.; Rao, L.; Wang, P.; Shi, Z.; Zhang, L. Photocatalytic activity of N-TiO_2/O-doped N vacancy g-C_3N_4 and the intermediates toxicity evaluation under tetracycline hydrochloride and Cr(VI) coexistence environment. *Appl. Catal. B Environ.* **2020**, *262*, 118308.